



HAL
open science

A new retroreflector named “quatriplan” based on the corner-cube principle, for advanced ultrasonic telemetry applications

Marie-Aude Ploix, Cécile Gueudré, Gilles Corneloup, François Baqué

► To cite this version:

Marie-Aude Ploix, Cécile Gueudré, Gilles Corneloup, François Baqué. A new retroreflector named “quatriplan” based on the corner-cube principle, for advanced ultrasonic telemetry applications. *Ultrasonics*, 2023, 132, pp.106999. 10.1016/j.ultras.2023.106999 . hal-04051806

HAL Id: hal-04051806

<https://hal.science/hal-04051806>

Submitted on 13 Feb 2024

HAL is a multi-disciplinary open access archive for the deposit and dissemination of scientific research documents, whether they are published or not. The documents may come from teaching and research institutions in France or abroad, or from public or private research centers.

L'archive ouverte pluridisciplinaire **HAL**, est destinée au dépôt et à la diffusion de documents scientifiques de niveau recherche, publiés ou non, émanant des établissements d'enseignement et de recherche français ou étrangers, des laboratoires publics ou privés.

15 **Abstract:**

16 Telemetry consists in remotely detecting and locating an object. For applications in immersed
17 structures as in nuclear primary vessel, ultrasonic waves are well adapted. Moreover, fixing a
18 target on the structures of interest maximizes the signal-to-noise ratio and provides a
19 reference point. Classical Corner-Cube Retroreflector (CCR) demonstrated high performance
20 in this framework (1D and 2D measurements) but does not allow knowing the full (3D)
21 positioning of the structure. This paper proposes an innovative compact target named
22 “quatriplan”, based on the CCR principle, and which must allow the ability to determine the
23 orientation of the target in addition to its distance to the transducer. The simple design of the
24 quatriplan is first explained, then its performances are investigated with modelling and
25 experimentations. The results highlight its strong performance and benefit for advanced
26 telemetry applications in industrial systems where complex design can impede easy and
27 efficient access for inspection of specific parts.

28

29 **Keywords:** Corner-Cube Retroreflector; trihedral; compact reflector; ultrasonic telemetry; 3D
30 geometrical positioning; acoustical target

31

32 **1. INTRODUCTION AND STATE-OF-THE-ART**

33 The improvement of in-service inspection and repair (ISI&R) is a major issue in the case of
34 (current and future) nuclear power plants. Ultrasonic solutions are particularly adapted to this
35 severe environment, in particular in the area of primary vessel. In this framework ultrasonic
36 telemetry aims at checking the actual presence of an internal structure, its position, its
37 potential deformation and/or its possible vibration, by measuring and monitoring relevant
38 distances. Attaching a target on the structure to be monitored helps improving signature and
39 detectability (e.g., in case of a misaligned or nonplanar structure, which would deviate the
40 beam, implying no reflection towards the transducer) and acquiring an interpretable signal
41 with an increased signal-to-noise ratio. Then knowing the time-of-flight of the waves and their
42 velocity, it is easy to calculate the corresponding distance.

43 The most efficient target is the Corner-Cube Retroreflector (CCR), also named trihedral
44 reflector. It consists of three mutually perpendicular, intersecting flat (mirror) surfaces, which
45 reflects waves directly towards the source, over a certain angular range. It is widely used since
46 the 1980s in the fields of electronics, optics and geophysics, e.g. for satellite/lunar ranging
47 systems (with laser) or earthquake monitoring applications (with radar waves) [1–8].

48 In the field of acoustics, only few work concerning retroreflectors were found in the literature
49 [9–14]. De Vadder and Lhémy [9] considered different retroreflectors, and proposed a
50 conical reflector for the purpose of improving the characterization of an ultrasonic beam.
51 Locqueteau [10] studied the reflectivity of different targets (sphere, disk and CCR, the latter
52 being identified as the best one), and developed more specifically diffraction analytic
53 modelling in order to rebuild the exact CCR diffraction diagram. It is furthermore mentioned
54 the use of CCR in SuperPhenix French reactor for ultrasonic telemetry measurements. Efforts
55 have continued at French CEA (Alternative Energies and Atomic Energy Commission) to model

56 diffraction by a scattering wedge [15]. Stephanis and Mourmouras [11] briefly proposed the
57 use of a CCR made in Perspex to perform distance measurement. Narayanan et al. [12]
58 perform amplitude and time-of-flight measurements on a CCR in order to evaluate the
59 absolute misalignment of an immersed focused transducer without need of priori calibration.
60 Finally Leysen et al. [13] developed a linear retroreflective surface (successive rectangular V-
61 shapes) with the aim of detecting lost objects, or more precisely detecting their shadow on
62 this reflective surface with a wide range of incidence angles.

63 Previous work of the authors [14] thoroughly investigated the acoustical properties of a CCR
64 and its potential when hidden behind plates, in immersion. They showed its ability to fully
65 reverse an incoming ultrasonic beam in the same direction at non-normal incidence, within
66 the angular range of $\pm 30^\circ$ in the case of a steel CCR immersed in water (reflection properties
67 are closely linked to the involved materials – examples are shown in the reference for steel
68 CCR in liquid sodium and copper CCR in water). It appeared possible to clearly locate the steel
69 CCR (and thus the structure on which it is attached) alone and hidden behind one and two
70 steel plates immersed in water.

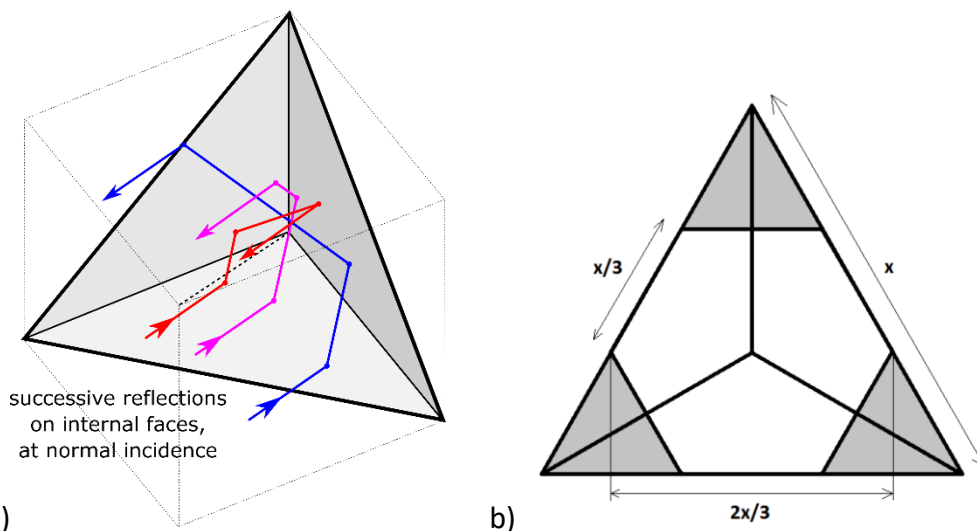
71 However, the use of this “classical” CCR only provides its distance to the ultrasonic transducer
72 and its lateral position in the plane perpendicular to the beam when scanning the area. It does
73 not allow measuring the eventual tilt of the structure. One possibility to overcome this
74 drawback is to fix several CCRs in an array for instance, as considered in [6,16] for optical
75 applications (lunar laser ranging). No similar development was found in the acoustics field in
76 the literature. In this framework, a new compact acoustical target named “quatriplan” is
77 developed and studied in this paper, following a patent filed by one of the authors [17]. Its
78 design is explained in section 2, then ultrasonic modelling and experimental work are exposed
79 in section 3, proving its great potential, which is further discussed in section 4.

80 Note that the precision will mainly depend on the equipment and processes used to evaluate
 81 time-of-flight, to measure ultrasonic velocity in the surrounding environment, and also on the
 82 chosen scan step. The size of the target has a fundamental influence: increasing its size will
 83 increase the resolution. Under the experimental conditions presented in this paper, an
 84 accuracy of $0,5^\circ$ is found (which means a displacement of 0,87 mm for 10 cm large structure).
 85 In the nuclear plant context, the size of the components to be controlled is large, which leads
 86 to specification on the displacements to measurement which are several tens of centimeters.
 87 So, this first result seems consistent for nuclear large-scale equipment.

88

89 **2. QUATRIPLAN TARGET DESIGN AND FABRICATION**

90 The key principle of a CCR is that an incoming wave is fully reversed in the same direction,
 91 after three successive reflections on each internal face (see examples on Figure 1a), within the
 92 angular range of $\pm 30^\circ$ (in case of steel in water) [14]; the incidence angle is defined relatively
 93 to the plane containing the three external edges of the CCR.

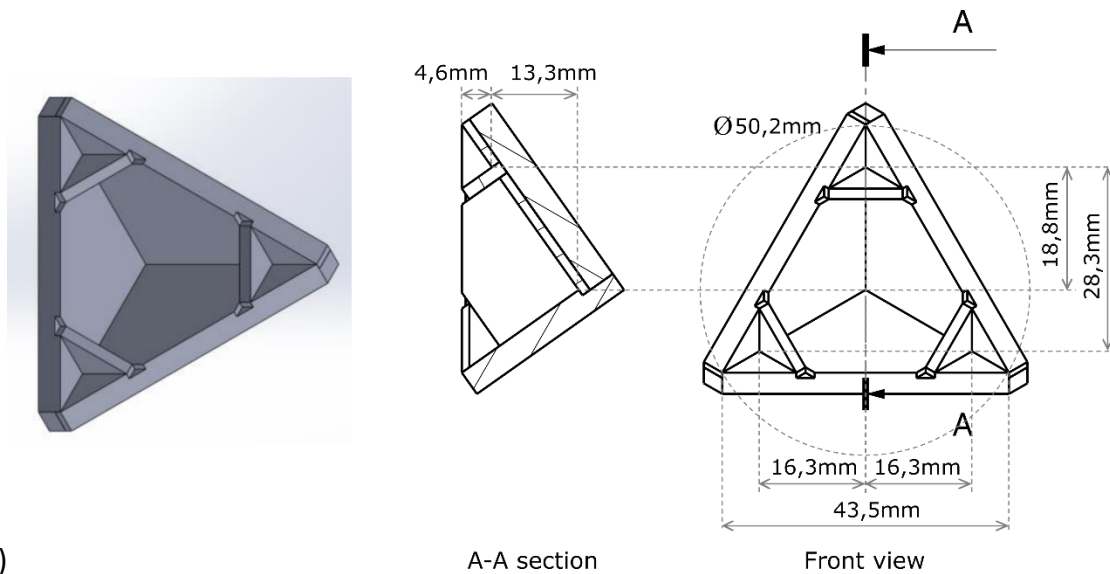


94

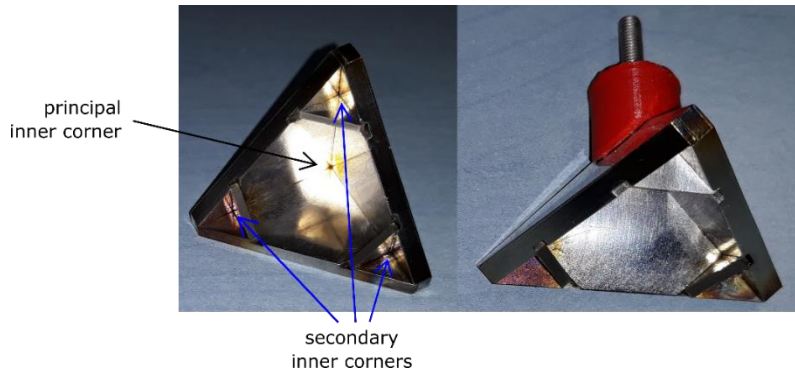
95 Figure 1: Illustration of the general principle of a CCR: a) Triple successive reflections of three rays at
 96 normal incidence; b) Effective (white) and shadow (gray) areas, from [4].

97 The design of the quatriplan is based around the idea that (1) several trihedral corners are
98 needed to obtain further positioning information, and (2) CCR presents ineffective (shadow)
99 areas since they reflect an incident ray only partially (one or two reflections instead of three).
100 Such areas for normal incidence [4,5] are the three triangular zones sizing a third of the CCR
101 edge length, located at the three endpoints of the CCR, as shown in Figure 1b (white zone is
102 the only zone where triple successive reflections mechanism occurs when CCR is normal to
103 the wavefront).

104 Thus, in the quatriplan design (presented in Figure 2a), three small corner cubes are added at
105 the three endpoints of the initial CCR. For this first mock-up made of steel, small triangular
106 plates are inserted at $\frac{1}{4}$ edge length (the aim is to work also with oblique incidence hence
107 effective and shadow areas will not remain exactly the previously described ones). On the
108 manufactured quatriplan (shown in Figure 2b), a support part (red part) with a threaded rod
109 is fixed behind the target so the target can be fixed on a plate in order to perform
110 measurements.



111 a)



112 b)

113 Figure 2: Drawing (a) and picture (b) of the quatriplan target.

114 In the following, the acoustical responses of the so-called principal and secondary inner
 115 corners are studied. Note that the dimensions of the external (principal) target are chosen
 116 identical to those of the CCR studied in [14] for the purpose of comparing their performance
 117 (material is also identical).

118

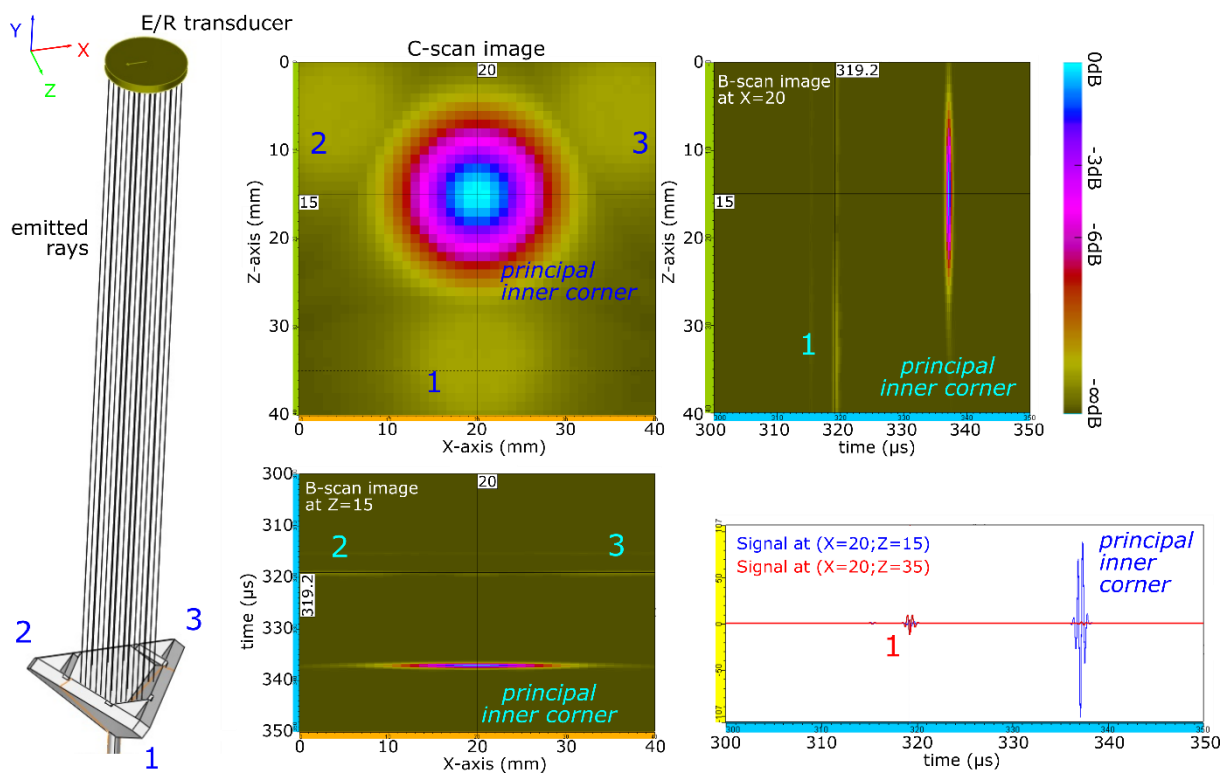
119 **3. ULTRASONIC PRELIMINARY MODELLING, AND EXPERIMENTAL ANALYSIS**

120 **3.1. CIVA modelling**

121 The first step of the study of the quatriplan potential and its acoustical properties involves
 122 modelling. This stage was performed before fabrication of the first quatriplan mock-up. The

123 CIVA platform is utilized here to model the ultrasonic beam reflection on quadriplan with
 124 normal and oblique incidence (equivalent to a tilt of the target). UT (Ultrasonic Testing)
 125 module of CIVA [18] allows bulk wave beam field predictions using the elastodynamics pencil
 126 method, and flaw response predictions, and can model many bulk wave inspection scenarios
 127 including A-scan, B-scan, C-scan, and S-scan.

128 The quadriplan CAD drawing was imported in CIVA, and an ultrasonic transducer (flat, 1"-
 129 diameter, broadband with 2,25 MHz central frequency) with the same characteristics as that
 130 used experimentally, is positioned at 250 mm from principal inner corner (along Y-axis), and
 131 operates as a pulser-receiver (see left drawing of Figure 3).



132

133 Figure 3: CIVA modelling: 2D scanning along X and Z-axis, with normal incidence.

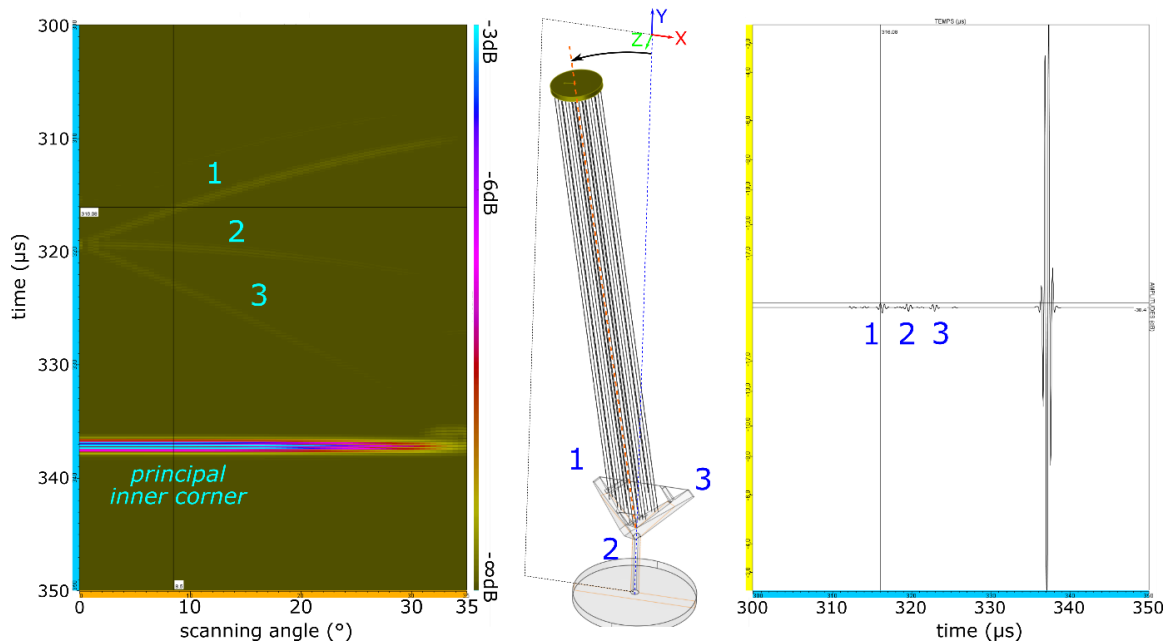
134 The first simulation consists in a 2D scanning (C-scan type) of the transducer with normal
 135 incidence, along X and Z-axis. The results are represented in Figure 3: the C-scan image
 136 represents the maximal amplitudes received at each point, two B-scan images are extracted,

137 representing the juxtaposition of the received signals on a scanning line, and two individual
138 signals are also plotted, one at the maximal amplitude from the principal CCR and the second
139 at the maximal amplitude from the secondary CCR numbered "1". The three secondary CCRs
140 are clearly identified around the principal inner corner. Their maximal reflected amplitudes
141 are about a tenth of that reflected by the principal CCR, and their echoes arrive about $18\mu\text{s}$
142 ahead of that of the principal CCR.

143 Note that, as highlighted by [4,5] in case of radar waves, the level of reflected amplitude
144 depends on the size of the target, compared to the size of the incident beam.

145

146 The second simulation launched, presented in Figure 4, consists in an angular scanning of the
147 transducer around the Z-axis and centred on the principal inner corner point. The results show
148 that, as for the simple CCR [14], the principal inner corner of the quadriplan sends back to the
149 transducer a maximum amplitude at 0° and a decrease is then observed until about 35° . The
150 echoes of the three secondary inner corners are clearly visible despite their low amplitude.
151 Their amplitude presents the same behaviour as that of the principal corner: maximal at 0°
152 and decreasing until about 35° . Their times-of-flight progressively separate when increasing
153 incidence angle, thus there are individually distinguishable.



154

155

Figure 4: CIVA modelling: angular scanning around Z-axis and principal inner corner point.

156

3.2. Experimental ultrasonic field reflected by quatriplan

157

3.2.1. With normal incidence

158

159

160

161

162

163

164

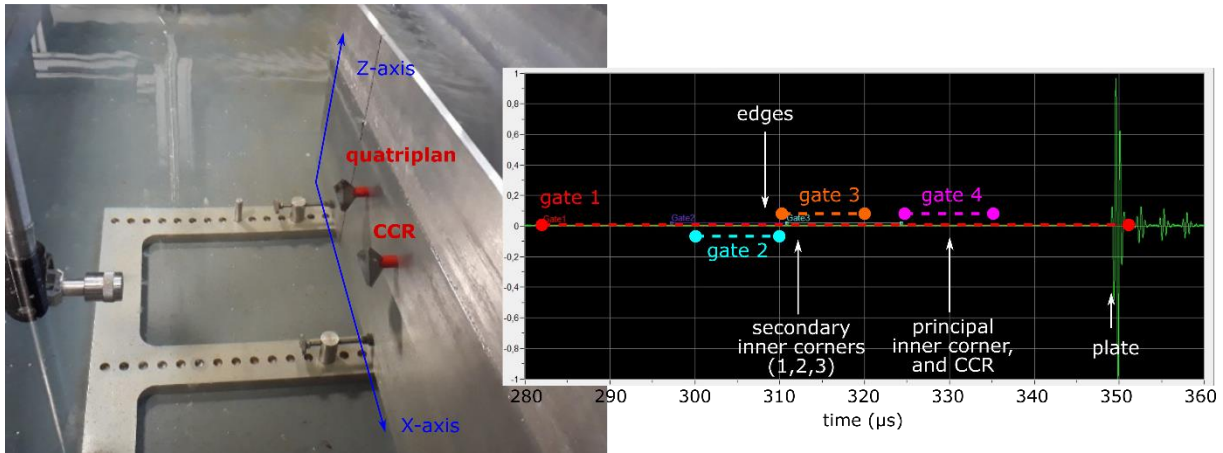
165

166

167

168

The first measurement campaign consists in acquiring and comparing the ultrasonic responses of the quatriplan and of a classical CCR, with normal incidence in water. As shown in the picture of Figure 5, they are both fixed on a plate and the ultrasonic pulser/receiver (flat, 1"-diameter, 2,25 MHz central frequency, positioned at 260mm from the plate) performs a 2D scan along X and Z-axis (with 1mm step in both directions). Different echoes are reflected towards the transducer, with different times-of-flight (see signal on right of Figure 5): the reflection on the plate, at about 350 μ s, the reflections of the inner corner of CCR and of the principal inner corner of quatriplan, at about 330 μ s, the reflections of the secondary inner corners of quatriplan, at about 312 μ s, and the diffraction on the edges of both targets, at about 309 μ s. That defines the four temporal gatings (numbered in Figure 5) performed afterwards to analyse the different reflections.



169

170 Figure 5: Experimental setup at normal incidence, and positions of the four time-domain gatings for
 171 signal processing

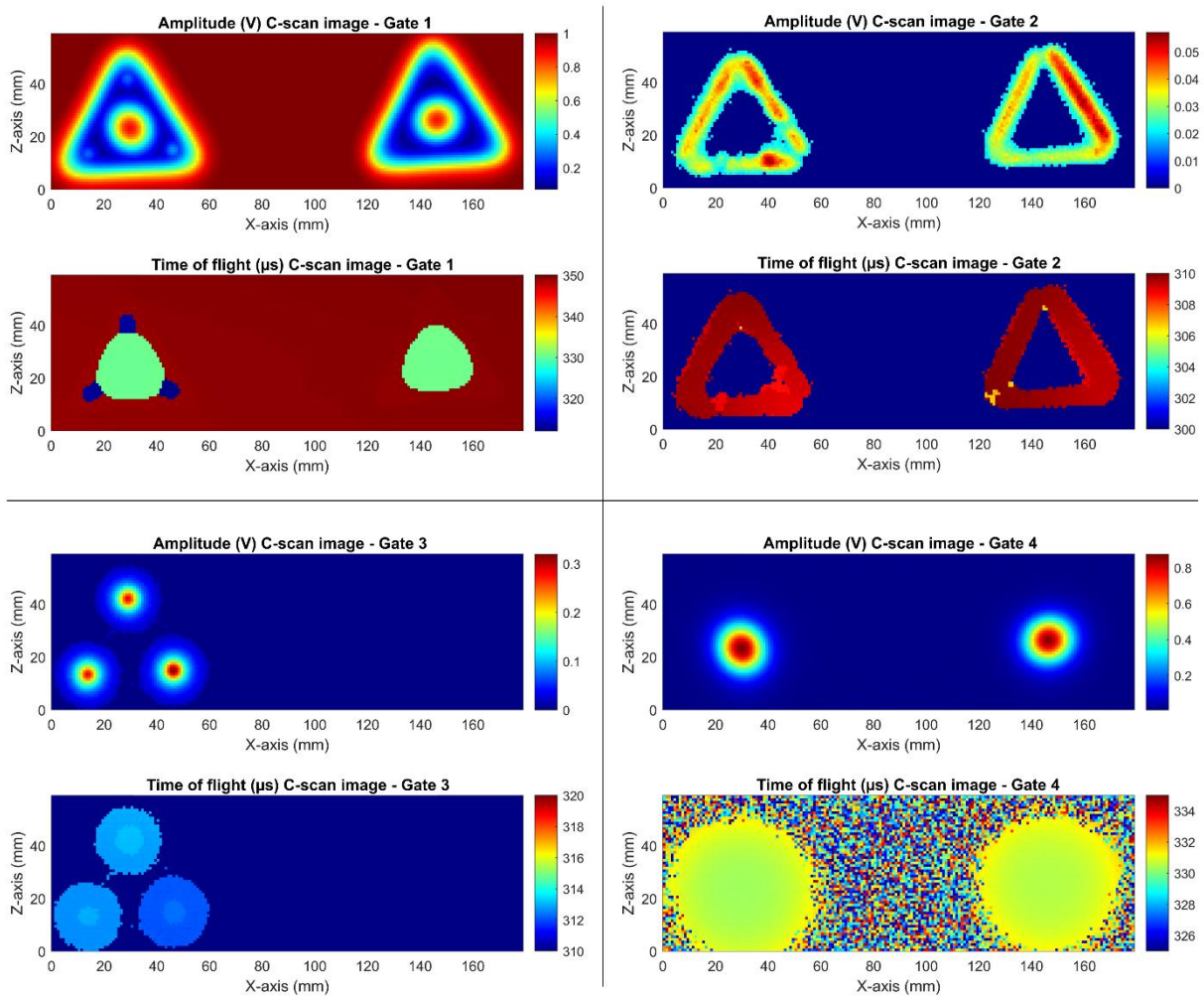
172 Figure 6 illustrates the resulting C-scan images in the four different temporal windows, in
 173 terms of maximal amplitude and associated time-of-flight.

174 - The first (global) gating highlights all the maximal echoes whatever their time-of-flight. CCR
 175 as well as quatriplan are clearly identified in the amplitude image as well as in the time-of-
 176 flight image. Moreover, secondary inner corners of quatriplan are also revealed without
 177 ambiguity, both in the amplitude and time-of-flight images.

178 - The second gating, focusing on the edges, highlights the diffraction echoes of the edges, with
 179 a low amplitude (about 5% of the principal inner corner amplitude). Echoes from the edges of
 180 the quatriplan seem more irregular than those of the CCR, and the additional edges of the
 181 secondary targets are not detectable. A slight inclination of the quatriplan with respect to the
 182 plate is here observable through the non-constant time-of-flight of diffraction echoes along
 183 the edges.

184 - The third gating emphasizes the echoes of the secondary inner corners. The slight difference
 185 of their times-of-flight confirms the slight misalignment of the quatriplan with respect to the

186 plate. The kind of halo around central time-of-flight map of each secondary CCR is due to a
 187 slight modification of the echo pattern, leading to a $\frac{1}{2}$ period drop of the maximum.
 188 - Finally, the last gating shows that the principal inner corner has the same acoustical response
 189 as the CCR one, with identical maximal amplitude and identical distributions in amplitude and
 190 time-of-flight.



191
 192 Figure 6: Amplitude and time-of-flight C-scan images for the four temporal windows (in each image,
 193 the quatriplan is on the left and the CCR on the right).

194 Table 1 provides the quantitative data in terms of position, amplitude and time-of-flight of
 195 each maximum, and deduced distance between the transducer and each inner corner.
 196 Reported times-of-flight correspond here to the arrival time of each maximum amplitude.

197 Results show first that the maximal amplitude reflected by the secondary corners is about 1/3
 198 maximal amplitude of the principal inner corner. They are then detected and identified
 199 without any ambiguity.

200

	(X,Z) position of the max. amplitude (mm)	Max. amplitude (V)	Time-of- flight (μ s)	Deduced distance ¹ transducer/max. point (on Y-axis) (mm)
CCR inner corner	(147;27)	0,87	330,50	246,2
Principal inner corner	(30;24)	0,87	330,33	246,1
Secondary inner corners:				
Quatriplan	Top	(29;43)	0,28	313,10
	Bottom-left	(14;14)	0,28	312,95
	Bottom-right	(47;15)	0,28	312,35

201 Table 1: Position, amplitude and time-of-flight of the maximum amplitude from each inner corner

202 Calculating afterwards each distance to the transducer based on each time-of-flight provide
 203 the complete spatial position of each inner corner. The discrepancies of a few tenths of mm
 204 confirm the slight inclination of the quatriplan with respect to the plate. One can determine
 205 the equation of the plane containing these three points (here: $11,8(X - 14) + 942(Y - 233,1) - 12,6(Z - 14) = 0$), and therefore calculate the global inclination of the quatriplan
 206 relatively to the plate surface plane (parallel to the plane of equation $Y = 0$), which is found
 207 here equal to $1,05^\circ$. This could also be due to the fabrication of the quatriplan, performed with
 208 the best possible accuracy, but some deviations from the original plan are inevitable. No
 209

¹ With a velocity of 1,49 mm/ μ s in water

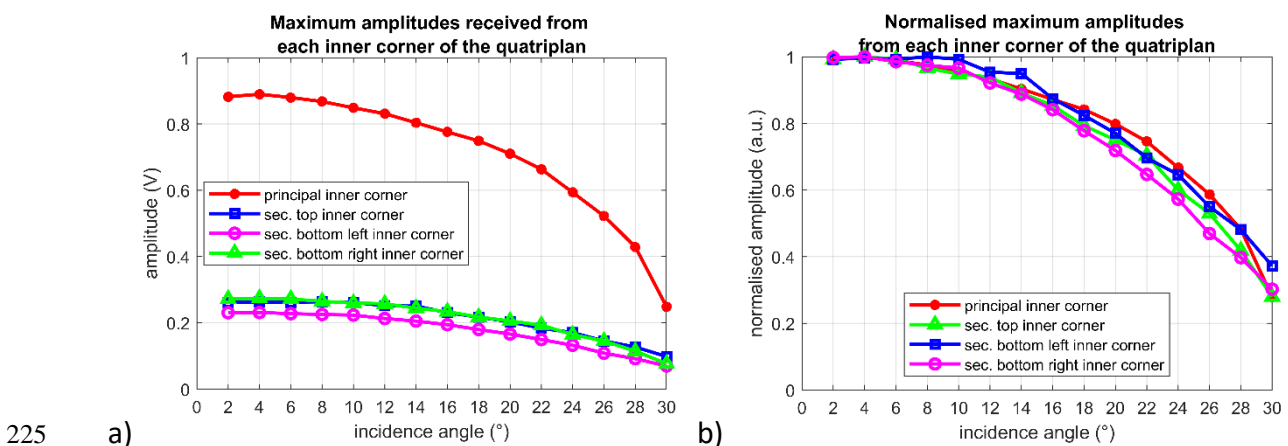
210 consequence exists in the context of industrial use, since measurements (especially in the
211 nuclear field) are always made relative to a saved initial measurement.

212

213 3.2.2. With oblique incidence

214 For the second set of measurements, the transducer is tilted, from 2° to 30° with a step of 2°,
215 and performs as previously a 2D scanning of the quatriplan. The objective in this paragraph is
216 to analyze and compare the acoustical responses of the principal and secondary inner corners
217 (the aspect of tilt evaluation will be discussed in the next section).

218 The main conclusion is that the secondary inner corners present the same behavior as the
219 principal one, and as a classical CCR. They are all identified whatever angle of incidence (in the
220 studied angle range), from amplitude and time-of-flight point of view. Figure 7 plots their
221 respective maximal amplitudes and illustrates on the normalized figure the similar behavior
222 of the different inner corners. Secondary inner corners send back sufficient energy over a wide
223 angular range to be potentially used for estimating the possible tilt of the quatriplan, and then
224 of the structure supporting it.



225 a)

b)

226 Figure 7: (a) Absolute and (b) normalized maximum amplitude received from each inner corner, in
227 oblique incidence.

228 **4. EVALUATION OF THE QUATRIPLAN TILT AND DISCUSSION**

229 To test experimentally the principle of tilt evaluation, a rotation (tilt) around the Z-axis of
230 Figure 5 is applied to the plate supporting the quadriplan. The angle was acoustically measured
231 (by adjusting the transducer so that the beam is normal to the plate, and reading the necessary
232 rotation) and equals $8,8^\circ$. This rotation was combined, in a CAD software (SolidWorks®), with
233 the slight inclination of the quadriplan relative to the plate measured previously, and the
234 resulting disorientation of the quadriplan relative to the transducer is of $8,2^\circ$. It is this angle
235 that is searched in the following.

236 Two procedures are then possible to evaluate the tilt, depending on whether scanning is
237 possible or not (for industrial application): either the position of the transducer is fixed, and
238 all echoes are extracted and analysed from a single signal, or a scanning is performed to find
239 the maximum echoes from each inner corner (as already realized above for normal incidence).

240

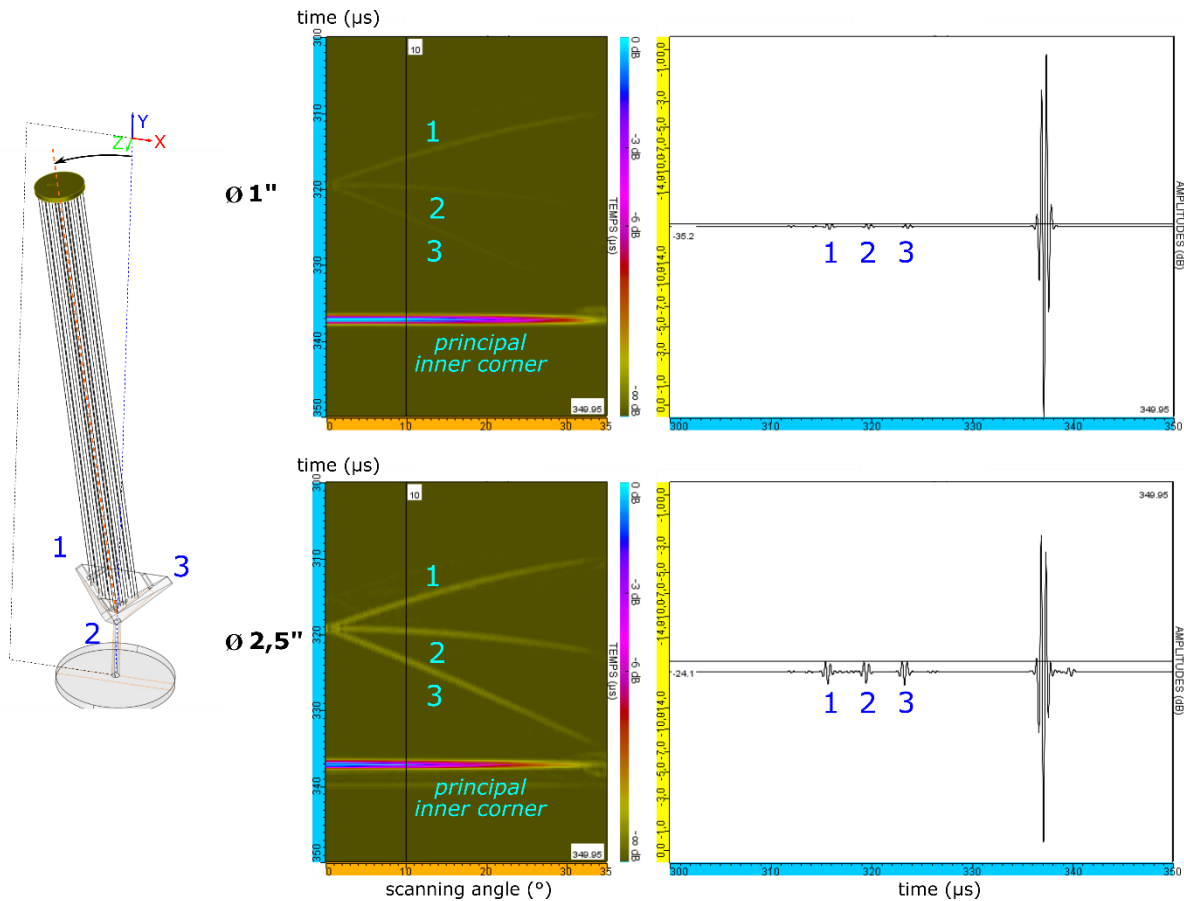
241 **4.1. From a single transducer position**

242 It involves the coexistence of all the echoes in a single signal, including those of the three
243 secondary inner corners. Thus, the incident beam must be large enough to “view” them
244 simultaneously. The previous setup does not allow this coexistence. For this issue, either a
245 larger transducer is operated, or the current transducer ($\varnothing 1''$) is moved back to take benefit
246 of the beam aperture in far-field.

247

248 The first solution is tested with modelling using CIVA. Results show (see Figure 8) that using a
249 $2,5''$ transducer results in a significant gain of about 15 dB on the echoes of secondary inner
250 corners compared to the principal one. But this kind of transducer is less common.

251



252

253

Figure 8: CIVA modelling with angular scanning, with 1" (top) and 2,5" (bottom) transducers

254

The second solution is tested experimentally: for the used transducer (1", 2,25 MHz), the -6dB

255

beam diameter reaches 50 mm at about 800 mm from the transducer. The transducer is then

256

moved back to about 870 mm (maximum tank capacity) from the (tilted) quadriplan and

257

adjusted to face the principal inner corner. The registered signal, plotted in Figure 9, highlights

258

all the echoes, clearly separated. At this distance, the secondary corners send back about 10-

259

12% of energy compared to that of the principal corner. The time-of-flight of each of them can

260

be recorded and allows inferring to the distance of each corner to the transducer.

261

The drawback of the procedure with a single transducer position is that it is not possible to

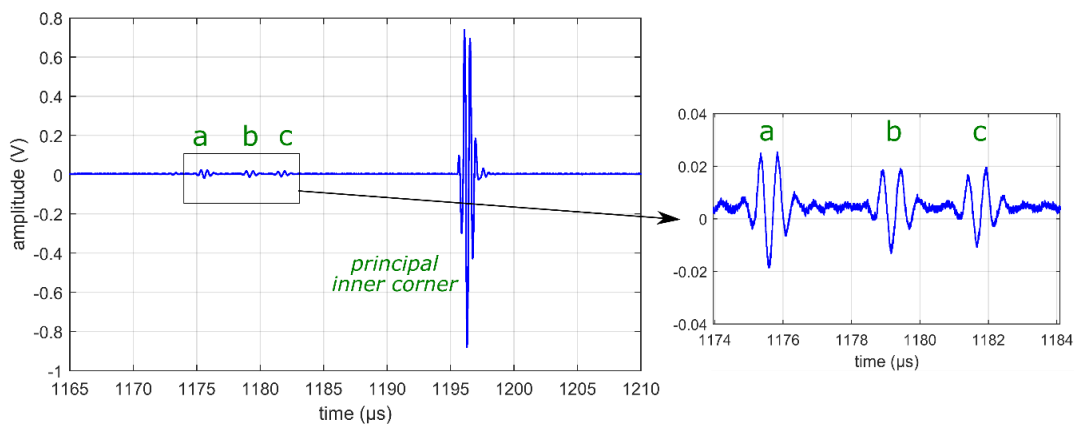
262

link an echo with one corner. Then one degree-of-freedom will remain unknown, which is the

263

rotation around the axis of revolution of the transducer (what will be known are the distances

264 of the different inner corners to the transducer). But this procedure can however be
 265 interesting to check if a tilt exists, and to evaluate a global tilt.



266

267 Figure 9: Signal acquired at about 870 mm from the tilted quadriplan.

268 Here, the chosen solution to estimate the tilt angle consists in entering the measured
 269 distances reported in Table 2 in SolidWorks® software, and then measure the global
 270 inclination of the quadriplan. Considering the transducer as a point source (conical beam), the
 271 measured angle is of 8,0°, and considering plane wave hypothesis (planar source), the
 272 measured angle is of 7,9°. These results are satisfactory compared to 8,2°.

273

	Max. amplitude (V)	Time-of-flight (μs)	Deduced distance transducer - max. point (mm)
Principal inner corner	0,88	1 196,3	891,2
Secondary inner corners:			
a	0,02	1 175,58	875,8
b	0,01	1 179,17	878,5
c	0,01	1 181,67	880,3

274 Table 2: Position, amplitude and time-of-flight of the maximum amplitude from each inner corner
 275 in the tilted configuration

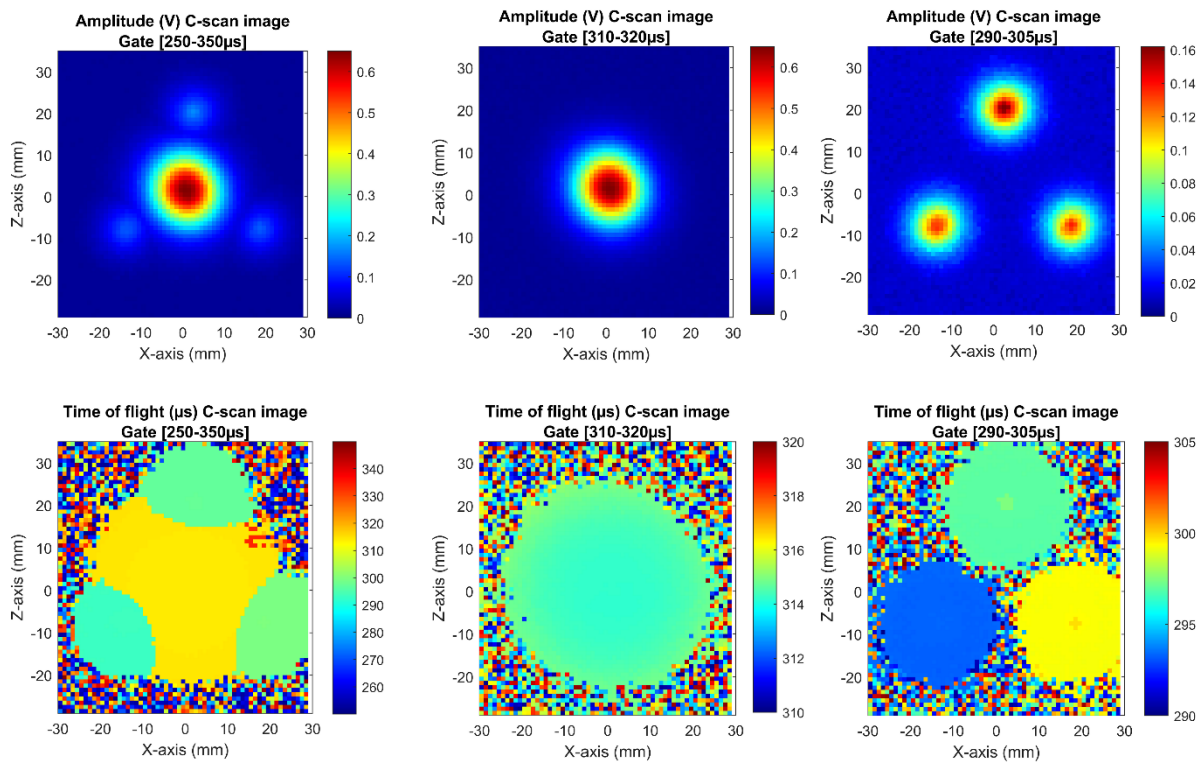
276 Note that this experimental procedure works properly only if the echoes are temporally well-
277 separated (“sufficient” tilt), or perfectly superimposed (no tilt).

278

279 4.2. With transducer scanning

280 For the second procedure, a 2D scanning (always along X and Z-axis, with 1mm step) is now
281 performed on the tilted quadriplan (and plate). The resulting C-scan images in amplitude and
282 time-of-flight are represented in Figure 10.

283 The first gating is global, and do not make appear the plate in contrast with previous results
284 (in Figure 6). The second gating around the time-of-flight of the principal inner corner enables
285 to check its acoustical response that is still similar to a “simple” CCR. Finally, the last gating is
286 around the times-of-flight of the secondary inner corners. Their echo amplitudes are here
287 between 20% and 25% of the principal one, and their times-of-flight are clearly different from
288 each other.



289

290 Figure 10: Amplitude and time-of-flight C-scan images on tilted quadriplan at about 230mm

291 As previously, one can extract the positions and times-of-flight of each maximum amplitude,
 292 reported in Table 3. The equation of the plane containing the three secondary inner corners
 293 can be calculated $(139(X + 14) - 912(Y - 218,5) + 20,8(Z + 9) = 0)$, and then a
 294 disorientation of about $8,7^\circ$ is found relative to $Y = 0$ plane.

295

	(X,Z) position of the max. amplitude (mm)	Max. amplitude (V)	Time-of- flight (μ s)	Deduced distance transducer - max. point (on Y-axis) (mm)
Principal inner corner	(0;0)	0,65	314,22	234,1
Secondary inner corners:				
Top	(2;20)	0,17	297,47	221,6
Bottom-left	(-14;-9)	0,13	293,35	218,5
Bottom-right	(18;-8)	0,14	299,81	223,4

296 Table 3: Position, amplitude and time-of-flight of the maximum amplitude from each inner corner
 297 in tilted configuration

298 Note that this scanning procedure allows complete locating of the quatriplan in the 3D space,
 299 contrary to the procedure with a single position of transducer.

300

301 5. CONCLUSION

302 In the framework of ultrasonic telemetry, an enhanced target named quatriplan is proposed
 303 and studied acoustically using modelling and experimentations. The benefit of its design,
 304 compared to the “simple” CCR, is that it allows to determine the orientation of the target in
 305 addition to its distance to the transducer, and then of the structure supporting it. It consists
 306 of a principal CCR with small secondary CCRs in its corners. Thus, the quatriplan has a simple

307 but highly efficient design: its acoustical response was analysed and shows a great potential.
308 Thorough modelling and experimentations on a first mock-up provide validation of the
309 possible estimation of positioning and tilting of the target and hence of the structure
310 supporting it. Small discrepancies were found in this study, certainly attributable to the non-
311 perfect fabrication and positioning of the quadriplan on the plate. This shows that a prior
312 calibration is necessary, as for any metrology process. But whatever the measurement, in
313 particular in nuclear field, this prior calibration is always performed in order to make
314 afterwards relative measurements and/or monitoring. Further improvements or adaptations
315 could however be made, in particular in terms of dimensions, depending on the intended
316 application.

317 This is a great advance for ultrasonic telemetry, in water as shown here but also in the case of
318 opaque liquids (as liquid sodium etc.). Moreover, as studied previously for CCR, the quadriplan
319 may be used behind screen(s) to measure or monitor 3D movements of "hidden" structures.
320 Thus many applications could take a large benefit of such an advanced acoustical reflector.

321

322 **ACKNOWLEDGEMENTS**

323 This research was supported by the French Alternative Energies and Atomic Energy
324 Commission (CEA) of Cadarache in the framework of the studies for improving In Service
325 Inspection for Generation IV Nuclear Reactors, and within the framework of the MISTRAL joint
326 research laboratory between Aix-Marseille University, CNRS, Centrale Marseille and CEA.

327

328 **REFERENCES**

- 329 [1] C. Li, J. Yin, J. Zhao, G. Zhang, X. Shan, The selection of artificial corner reflectors based on RCS
330 analysis, *Acta Geophys.* 60 (2012) 43–58. <https://doi.org/10.2478/s11600-011-0060-y>.
- 331 [2] X.-J. Shan, J.-Y. Yin, D.-L. Yu, C.-F. Li, J.-J. Zhao, G.-F. Zhang, Analysis of artificial corner reflector's
332 radar cross section: a physical optics perspective, *Arab. J. Geosci.* 6 (2013) 2755–2765.
333 <https://doi.org/10.1007/s12517-012-0582-x>.
- 334 [3] Y. Qin, D. Perissin, L. Lei, The Design and Experiments on Corner Reflectors for Urban Ground
335 Deformation Monitoring in Hong Kong, *Int. J. Antennas Propag.* 2013 (2013) 1–8.
336 <https://doi.org/10.1155/2013/191685>.
- 337 [4] M.C. Garthwaite, S. Nancarrow, A. Hislop, M. Thankappan, J.H. Dawson, S. Lawrie, The Design of
338 Radar Corner Reflectors for the Australian Geophysical Observing System: a single design
339 suitable for InSAR deformation monitoring and SAR calibration at multiple microwave frequency
340 bands., *Geosci. Aust.* (2015). <https://doi.org/10.11636/Record.2015.003>.
- 341 [5] E.F. Knott, J.F. Schaeffer, M.T. Tulley, *Radar Cross Section*, SciTech Publishing, 2004.
- 342 [6] T. Wang, W. Wang, P. Du, D. Geng, X. Kong, M. Gong, Calculation of the light intensity
343 distribution reflected by a planar corner-cube retroreflector array with the size of centimeter
344 and above, *Opt. - Int. J. Light Electron Opt.* 124 (2013) 5307–5312.
345 <https://doi.org/10.1016/j.ijleo.2013.03.056>.

- 346 [7] Y. Weng, S. Li, H. Zhou, J. Yang, G. Zheng, P. Zhang, Research on far-field diffraction of cube-
347 corner retroreflector in the satellite laser ranging system, in: 5th Int. Symp. Adv. Opt. Manuf.
348 Test. Technol. Opt. Test Meas. Technol. Equip., 2010: pp. 76564R-76564R-8.
349 <https://doi.org/10.1117/12.865518>.
- 350 [8] Y. He, Q. Liu, H.-Z. Duan, J.-J. He, Y.-Z. Jiang, H.-C. Yeh, Manufacture of a hollow corner cube
351 retroreflector for next generation of lunar laser ranging, *Res. Astron. Astrophys.* 18 (2018) 136.
352 <https://doi.org/10.1088/1674-4527/18/11/136>.
- 353 [9] D. Devadder, A. Lhemery, New Reflector for Experimental Characterization of Ultrasonic
354 Transducers, *J. Phys.* 51 (1990) 1295–1298. <https://doi.org/10.1051/jphyscol:19902304>.
- 355 [10] C. Locqueteau, Etude des cibles triplanes utilisées en télémétrie ultrasonore (Study of triplane
356 targets used in ultrasonic telemetry), PhD, Université d’Aix-Marseille II. Faculté des sciences,
357 1992.
- 358 [11] C.G. Stephanis, D.E. Mourmouras, Trihedral rectangular ultrasonic reflector for distance
359 measurements, *NDT E Int.* 28 (1995) 95–96. [https://doi.org/10.1016/0963-8695\(94\)00012-9](https://doi.org/10.1016/0963-8695(94)00012-9).
- 360 [12] M.M. Narayanan, N. Singh, A. Kumar, C. Babu Rao, T. Jayakumar, An absolute method for
361 determination of misalignment of an immersion ultrasonic transducer, *Ultrasonics.* 54 (2014)
362 2081–2089. <https://doi.org/10.1016/j.ultras.2014.06.021>.
- 363 [13] W. Leysen, M. Dierckx, D. Van Dyck, Development and applications of retroreflective surfaces for
364 ultrasound in LBE, in: 4th Int. Conf. Adv. Nucl. Instrum. Meas. Methods Their Appl. ANIMMA,
365 Ieee, Lisbon (Portugal), 2015. [https://www.webofscience.com/wos/woscc/full-
366 record/WOS:000398710600010](https://www.webofscience.com/wos/woscc/full-record/WOS:000398710600010).
- 367 [14] M.-A. Ploix, P. Kauffmann, J.-F. Chaix, I. Lillamand, F. Baque, G. Corneloup, Acoustical properties
368 of an immersed corner-cube retroreflector alone and behind screen for ultrasonic telemetry
369 applications, *Ultrasonics.* 106 (2020) 106149. <https://doi.org/10.1016/j.ultras.2020.106149>.

- 370 [15] B. Lü, M. Darmon, L. Fradkin, C. Potel, Numerical comparison of acoustic wedge models, with
371 application to ultrasonic telemetry, *Ultrasonics*. 65 (2016) 5–9.
372 <https://doi.org/10.1016/j.ultras.2015.10.009>.
- 373 [16] M. Martini, S. Dell’Agnello, D. Currie, G. Delle Monache, R. Vittori, J.F. Chandler, C. Cantone, A.
374 Boni, S. Berardi, G. Patrizi, M. Maiello, M. Garattini, C. Lops, R. March, G. Bellettini, R. Tauraso, N.
375 Intaglietta, M. Tibuzzi, T.W. Murphy, G. Bianco, E. Ciocci, MoonLIGHT: A USA-Italy lunar laser
376 ranging retroreflector array for the 21st century, *Planet. Space Sci.* 74 (2012) 276–282.
377 <https://doi.org/10.1016/j.pss.2012.09.006>.
- 378 [17] F. Baqué, Cible ultrasonique pour le contrôle non destructif, FR3112399, 2022.
379 <https://data.inpi.fr/brevets/FR3112399?q=#FR3112399>.
- 380 [18] S. Mahaut, S. Chatillon, M. Darmon, N. Leymarie, R. Raillon, P. Calmon, An overview of ultrasonic
381 beam propagation and flaw scattering models in the civa software, *AIP Conf. Proc.* 1211 (2010)
382 2133–2140. <https://doi.org/10.1063/1.3362393>.
- 383

384 **FIGURES CAPTIONS**

385 Figure 1: Illustration of the general principle of a CCR: a) Triple successive reflections of three
386 rays at normal incidence; b) Effective (white) and shadow (gray) areas, from [4].

387 Figure 2: Drawing (a) and picture (b) of the “quatriplan” target.

388 Figure 3: CIVA modelling: 2D scanning along X and Z-axis, with normal incidence.

389 Figure 4: CIVA modelling: angular scanning around Z-axis and principal inner corner point.

390 Figure 5: Experimental setup at normal incidence, and time-domain gating for signal
391 processing

392 Figure 6: Amplitude and time-of-flight C-scan images for the four temporal windows.

393 Figure 7: (a) Absolute and (b) normalized maximum amplitude received from each inner
394 corner, in oblique incidence.

395 Figure 8: CIVA modelling with angular scanning, with 1” (top) and 2,5” (bottom) transducers

396 Figure 9: Signal acquired at about 870 mm from the tilted quatriplan.

397 Figure 10: Amplitude and time-of-flight C-scan images on tilted quatriplan at about 230mm

398

399

400 **TABLE CAPTIONS**

401 Table 1: Position, amplitude and time-of-flight of the maximum amplitude from each inner
402 corner

403 Table 2: Position, amplitude and time-of-flight of the maximum amplitude from each inner
404 corner in the tilted configuration

405 Table 3: Position, amplitude and time-of-flight of the maximum amplitude from each inner
406 corner in tilted configuration

407